

SOLEIL and ALMA views on prototypical organic nitriles: C₂H₅CN

Christian P. Endres^a, Marie-Aline Martin-Drumel^b, Oliver Zingsheim^c, Luis Bonah^c, Olivier Pirali^{b,d}, Tianwei Zhang (张天惟)^c, Álvaro Sánchez-Monge^c, Thomas Möller^c, Nadine Wehres^c, Peter Schilke^c, Michael C. McCarthy^e, Stephan Schlemmer^c, Paola Caselli^a, Sven Thorwirth^c

^aMax-Planck-Institut für extraterrestrische Physik, 85748 Garching, Germany

^bUniversité Paris-Saclay, CNRS, Institut des Sciences Moléculaires d'Orsay, 91405 Orsay, France

^cI. Physikalisches Institut, Universität zu Köln, Zülpicher Straße 77, 50937 Köln, Germany

^dSOLEIL synchrotron, AILES beamline, l'Orme des Merisiers, Saint-Aubin, F-91190 Gif-sur-Yvette, France

^eCenter for Astrophysics | Harvard & Smithsonian, 60 Garden St., Cambridge, MA 02138, U.S.A.

Abstract

The high resolution vibrational spectrum of ethyl cyanide (C₂H₅CN) has been investigated in the far-IR using synchrotron-based Fourier transform spectroscopy. The assignment was performed using the Automated Spectral Assignment Procedure (ASAP) allowing accurate rotational energy levels of the four lowest fundamental vibrations of the species, namely the $\nu_{13} = 1$ @ 205.934099(8) cm⁻¹, and $\nu_{21} = 1$ @ 212.141101(8) cm⁻¹, $\nu_{20} = 1$ @ 372.635293(15) cm⁻¹, $\nu_{12} = 1$ @ 532.699617(16) cm⁻¹ states, to be determined. The analysis not only confirms the applicability of the ASAP in the treatment of (dense) high-resolution infrared spectra but also reveals some of its limitations. Complementary to the infrared study, the pure rotational spectrum of C₂H₅CN was also studied in selected frequency ranges from 75 to 255 GHz.

New observations of a prototypical high-mass star-forming region, G327.3–0.6, performed with the Atacama Large Millimeter Array show that vibrational satellites of C₂H₅CN can be very intense, of order several tens of Kelvin in units of brightness temperature.

Keywords: Ethyl cyanide, Propionitrile, Synchrotron, Far-IR rotation-vibration, ALMA observations, G327.3–0.6

1. Introduction

Ethyl cyanide (propionitrile, C₂H₅CN) was first detected in space in 1977 by Johnson et al. [1] towards star-forming regions associated with the Orion nebula (Orion-KL) and the Galactic center (Sgr B2). Since these early days of radio astronomy, ethyl cyanide has been found in many astronomical sources and has turned into a useful diagnostic of regions of high- and of low-mass star formation [2]. In selected sources, the molecule is so abundant, that not only the parent isotopic species ¹²CH₃¹²CH₂¹²C¹⁴N but also singly substituted ¹³C species [3, 4], ¹⁵N species [5], doubly substituted ¹³C species [6], and possibly also deuterated species [7] were observed. As ethyl cyanide possesses several energetically low-lying vibrational modes, it has not only been detected in the ground vibrational but also in vibrationally excited states by radio astronomical means [8–10], more precisely, vi-

brational satellites from the CCN in-plane bending mode ν_{13} and the methyl torsional mode ν_{21} (both of which are located around 210 cm⁻¹) as well as the CCN out-of-plane bending mode ν_{20} (373 cm⁻¹) and the CCC bending mode ν_{12} (534 cm⁻¹) were assigned.

As a prototypical simple organic nitrile, and also to support astronomical observations, ethyl cyanide has been studied quite extensively in the laboratory probing its pure rotational spectrum up to frequencies as high as 1.6 THz in the ground vibrational state [Refs. 11–13, and references therein]. Micro-, millimeter- and submillimeter-wave techniques have also been applied to the study of vibrational satellites [see Refs. 9, 10, 14, 15, and references therein] and even to multiple substituted isotopic species [Ref. 16, and references therein]. However, up to now no sufficiently comprehensive and concise picture of the millimeter-/submillimeter wave vibrational satellite pattern has emerged from lab-

oratory studies to satisfy the needs from the astronomical community, particularly in view of the capabilities of the most powerful astronomical facilities such as the Atacama Large Millimeter Array, ALMA. Further scarcity is encountered when considering the status of infrared studies. While the infrared spectrum of ethyl cyanide (and selected isotopic species) has been studied at low spectral resolution in the gas phase and in inert gas matrices [e.g., Refs. 17–21], to some surprise, no high-resolution infrared measurements of any vibration mode have been reported so far.

In the present investigation, the first high resolution rotation-vibration spectra of ethyl cyanide have now been collected from 80 to 650 cm⁻¹ at the SOLEIL synchrotron facility by means of high resolution Fourier-transform infrared (IR) spectroscopy. The spectral analysis of the four lowest fundamental vibrational bands was performed using the Automated Spectral Assignment Procedure (ASAP) shown previously on several occasions to offer a fast and convenient way towards spectroscopic analysis of high-resolution infrared data [22–24]. Subsequently, to further complement the infrared study, the pure rotational spectrum was re-investigated in the frequency regions from 75 to 119.6 GHz and from 160 to 254.95 GHz using submillimeter-wave spectrometers from the Cologne institute.

Based on new predictions of the pure rotational vibrational satellite spectrum obtained from the new best-fit parameters sets, a number of very strong emission lines from vibrationally excited C₂H₅CN were assigned in the spectrum of a prototypical high-mass star-forming region, G327.3–0.6, obtained with the ALMA.

2. Experiment

2.1. Ro-vibrational measurements

Synchrotron-based far-infrared spectra of propionitrile were recorded in the 80–650 cm⁻¹ range on the AILES beamline of the SOLEIL synchrotron facility [25]. The Bruker IFS125 Fourier-transform interferometer of the beamline was configured with a 6 μm Mylar beamsplitter, an iris aperture of 1.5 mm, and set for its ultimate resolution, *i.e.*, 0.001 cm⁻¹. Vapor pressure of the ethyl cyanide sample was introduced into a White-type, multi-reflection cell aligned for about 150 m absorption

path length [26, 27]. A liquid-helium cooled Si bolometer was used for detection. Two spectra of ethyl cyanide (99 % purity; Aldrich), with sample pressures of 26 and 500 μbar and resulting from the co-addition of 240 and 130 interferograms, were recorded to maximise the signal-to-noise ratio of the ν₁₃/ν₂₁ and ν₂₀/ν₁₂ bands, respectively. Residual water lines, present in the spectra, have been used for calibration purposes; their frequencies were taken from Refs [28–30]. The resulting spectra are presented in Fig. 1.

A successful ASAP treatment via cross correlation plots requires that the parts of the spectrum where spectral features are absent—below the noise level or below the confusion limit—exhibit signal intensities close to zero. To do so, the experimental spectra are usually plotted in absorbance. In the present case, in order to fulfill this requirement, it was necessary to further process each of our absorption spectra. Indeed, as can be seen in Fig. 1, the bands are not fully resolved which results in an apparent continuum underlying each band, because of both the large line density and the inherent FT interferometer-limited instrumental resolution. To ensure an optimum ASAP treatment, an artificial background (corresponding to the absorption continuum mentioned above) has been removed from the plots (see Figs. 2, 3, and 4). This background has been derived by taking the smallest value of the signal intensity in the vicinity (± 0.006 cm⁻¹) of each frequency point. This signal processing improves the suppression of spectral features associated with other transitions present in one of the other portions of the spectrum involved in the multiplication.

2.2. Pure rotational measurements

The measurements in the millimeter-wavelength region were conducted in Cologne in the 75–120 GHz and 160–255 GHz regions using two similar experimental setups described in greater detail in Refs. [32, 33]. In both cases, the spectrometer follows a relatively simple format: a frequency source generates the millimeter-waves (radiofrequency synthesizer followed by frequency multiplier chains and horn antenna) which probe the chemical composition of the absorption cells and are further detected using Schottky-diode detectors. While the two aforementioned frequency regions could have been measured using one or the other spectrometer, the present choice was guided by the sake of simplicity, as each instrument was

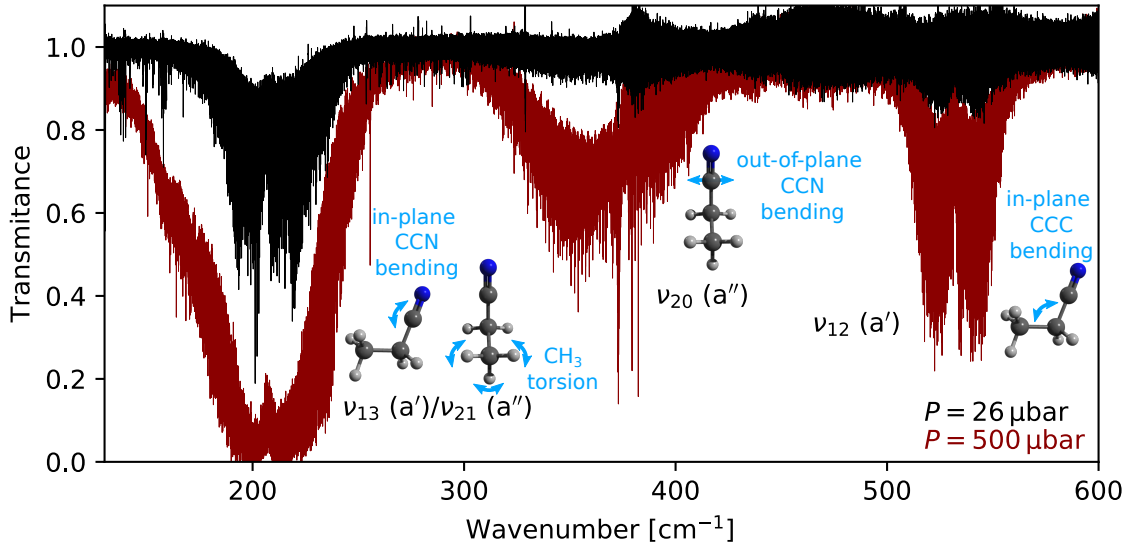


Figure 1: Overview of the far-IR spectra, presented in transmittance, recorded in this work with a pressure of 500 (in dark red) and 26 (in black) μbar . Strong lines of water and its isotopologues have been removed for the sake of clarity using HITRAN linelists [31]. The main motion associated with each vibration of the molecule is indicated by blue arrows.

already set for operating in one of each spectral range. The lower frequency range was measured using an absorption cell in single-pass mode with a total absorption path length of 14 m while the upper frequency one was investigated using a double-pass setup, adding up to a total absorption path length of 10 m. Because of the 2f modulation scheme, the resulting line shapes are close to a second derivative of a Gaussian function. Typical integration times were of 50 ms per frequency step. The step size was varied between 20 and 75 kHz, depending on the frequency ranges. All measurements were conducted at room temperature and ethyl cyanide (99 % purity; Aldrich) pressures of about 10 μbar . The spectra recorded in the upper frequency band is displayed in Fig. 5.

3. Theoretical Background

Ethyl cyanide is a prolate, asymmetric top molecule with one plane of symmetry defined by the heavy atom backbone (C_s). Due to its strong permanent dipole moment (of projections $\mu_a = 3.816 \text{ D}$, $\mu_b = 1.235 \text{ D}$ along the molecular-fixed principal axes [34]) the pure rotational spectrum shows strong a - and b -type transitions. Because of the internal rotation of the CH₃⁻ group relative to

the rest of the C_s frame, the symmetry is given by the molecular symmetry group G_6 and each rotational level is split into A and E symmetric substates. However, the barrier to torsion is quite high ($V_3 = 1075 \text{ cm}^{-1}$ [35]) thus the classification in terms of C_s symmetry of the rigid rotor limit remains useful. The A/E splitting in the vibrational ground state is barely resolved in Doppler limited measurements while doublets spaced by several MHz are typically observed for transitions within the first excited torsional state.

The vibrational spectrum of ethyl cyanide has been described in some more details in Wurrey et al. [18]. Briefly, the 21 fundamental vibrational modes, all of which are IR active, distribute as 13a' + 8a'' in which the a' and a'' vibrations correspond to in-plane and out-of-plane deformations with respect to the plane of symmetry, respectively. Consequently, the a' vibrations show hybrid a/b -type spectra whereas the a'' ones show c-type spectra. Four fundamental bands lie in the far-IR domain (see Fig. 6): the CCN in-plane bending mode ν_{13} around 206.9 cm⁻¹ [20], the torsional mode ν_{21} at 210.7 cm⁻¹ (estimated from combination bands) [19], the CCN out-of-plane bending mode ν_{20} around 373 cm⁻¹ [19], and the CCC deformation mode ν_{12} around 534.4 cm⁻¹ [19]. Numerous

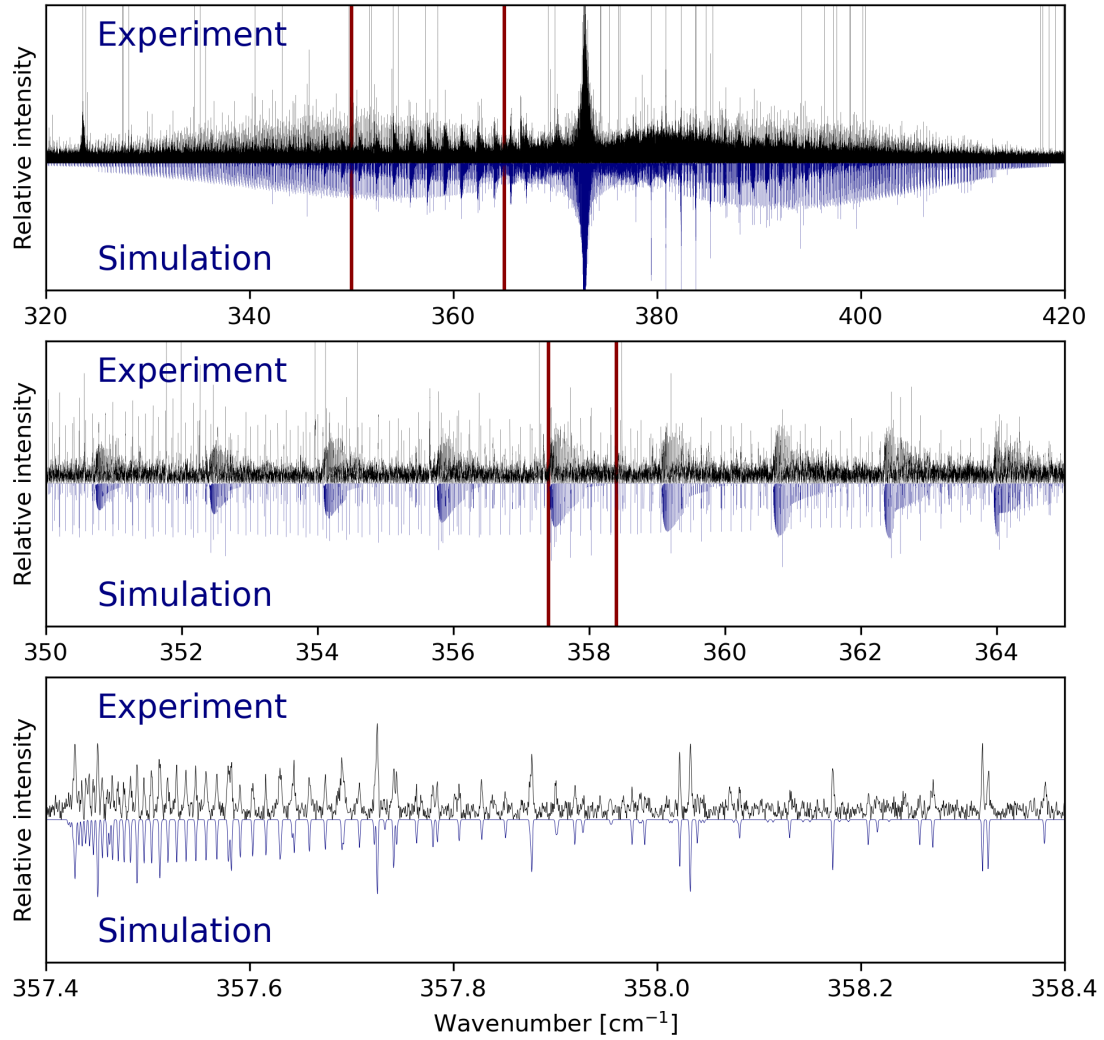


Figure 2: Experimental (post-processed, 500 μbar) and calculated (final set of parameters, this work) spectrum of the fundamental ν_{20} mode. Maroon vertical lines indicate the spectral range enlarged in the lower panels of the figure. The simulation is obtained by convolution of the predicted transitions (SPCAT) with a FWHM=0.0015 cm⁻¹ Gaussian profile.

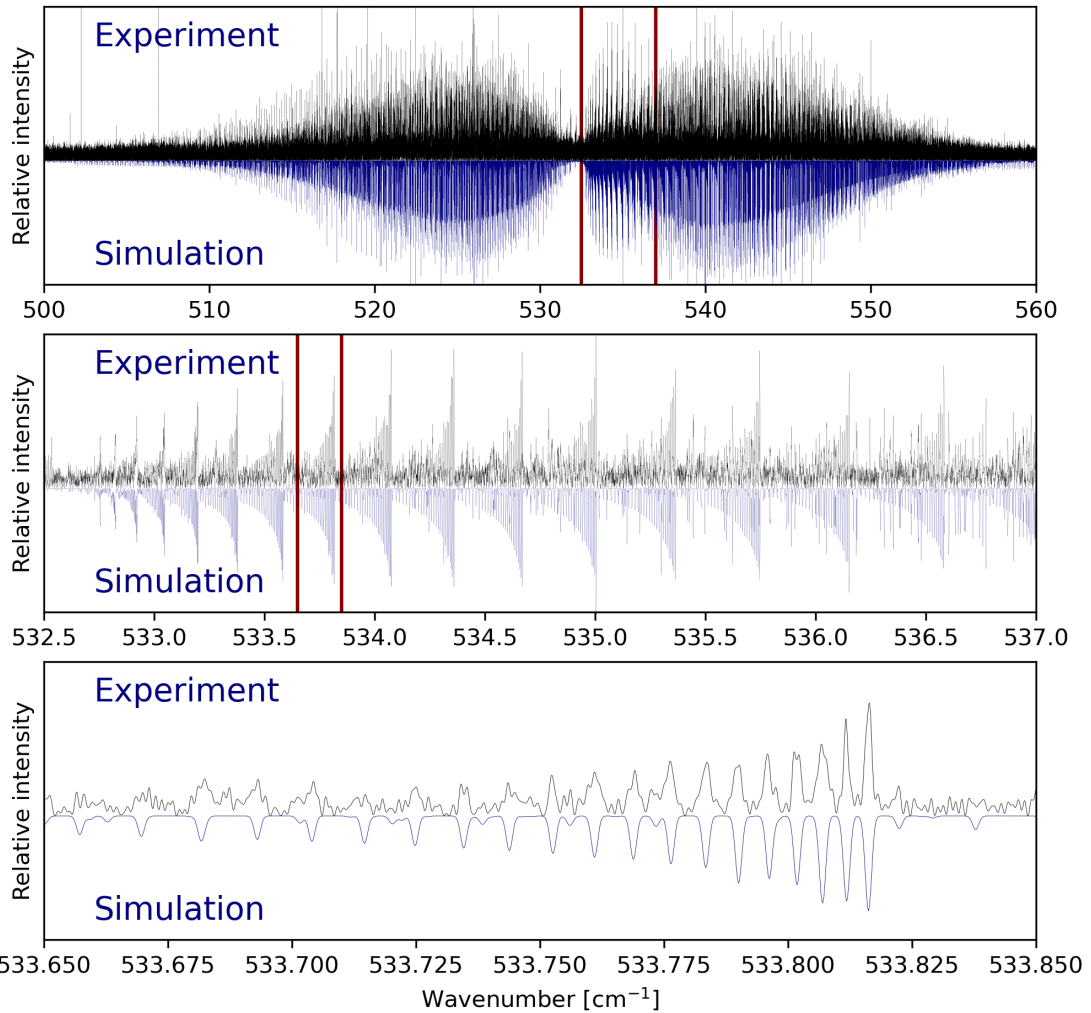


Figure 3: Experimental (post-processed, $500 \mu\text{bar}$) and calculated spectrum (final set of parameters, this work) of the fundamental ν_{12} mode. Maroon vertical lines indicate the spectral range enlarged in the lower panels of the figure. The simulation is obtained by convolution of the predicted transitions (SPCAT) with a FWHM=0.0015 cm^{-1} Gaussian profile.

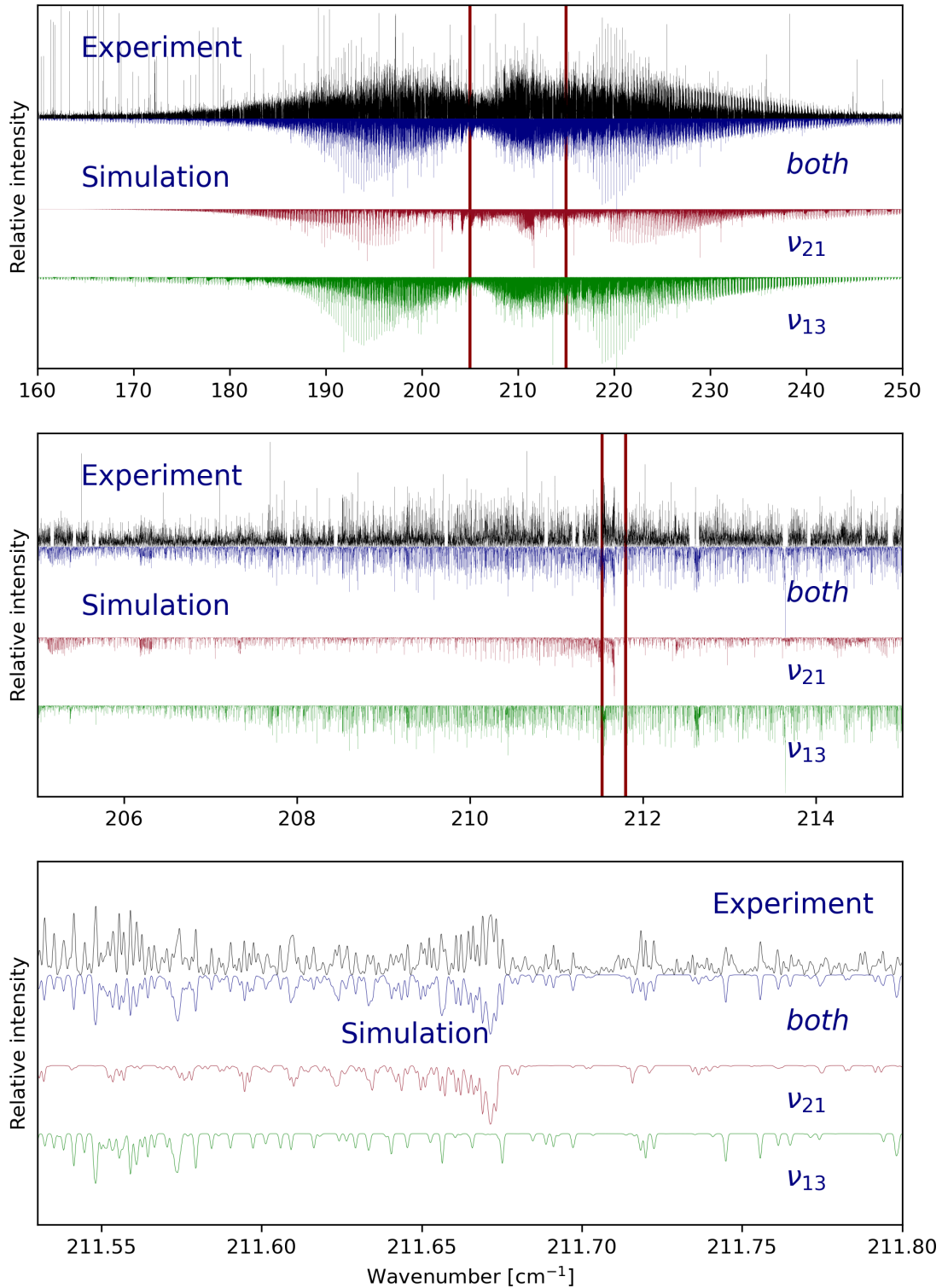


Figure 4: Experimental (post-processed, 26 μbar) and calculated (final set of parameters, this work) spectrum of the fundamentals ν_{21} and ν_{13} . Maroon vertical lines indicate the spectral range enlarged in the lower panels of the figure. The simulation is obtained by convolution of the predicted transitions (SPCAT) with a $\text{FWHM} = 9 \cdot 10^{-4} \text{ cm}^{-1}$ Gaussian profile. Narrow gaps in the experimental spectrum are due to removal of strong water lines.

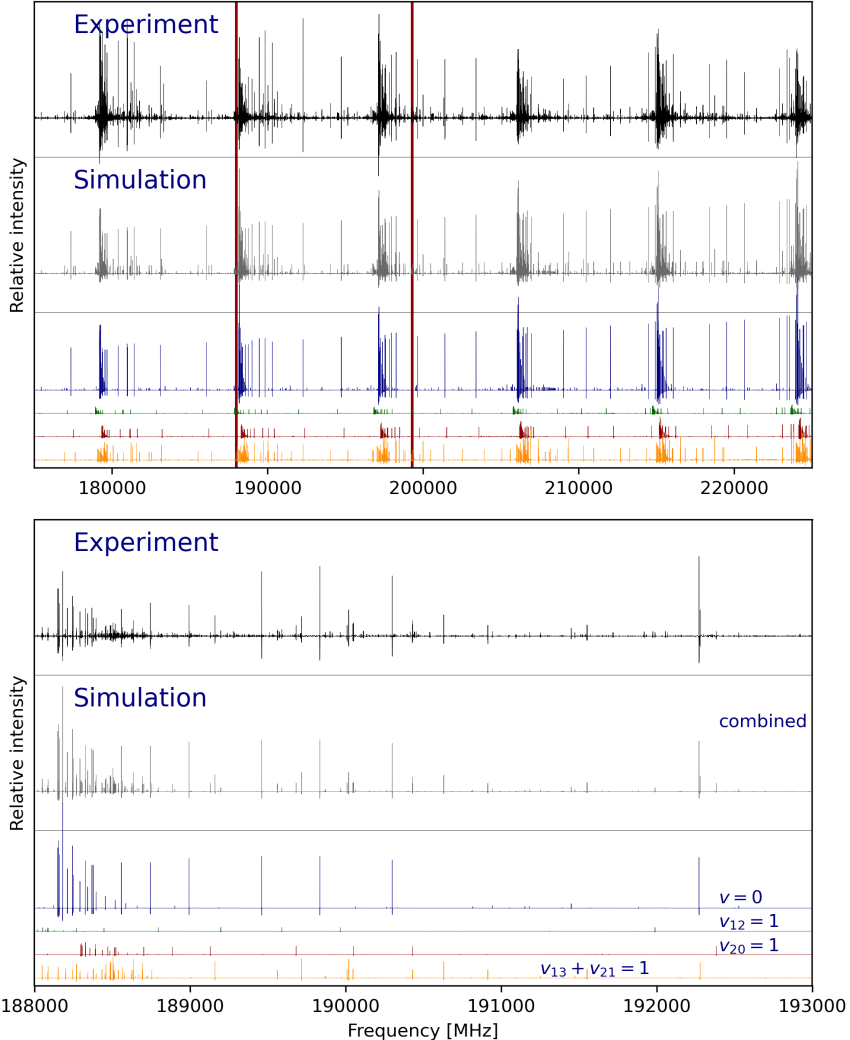


Figure 5: Experimental and calculated spectrum of pure rotational transitions in the ground vibrational state (blue) and $v_{12} = 1$ (green), $v_{20} = 1$ (red), and $v_{13} = 1$ and $v_{21} = 1$ (yellow, same plot) excited states. The combined simulation of all vibrational states is shown in grey. The simulation is obtained by convolution of the predicted transitions (SPCAT) with the second derivative of Gaussian profile.

and partially strong interactions are observed between these low-energy vibrational states [10, 36].

A number of effective Hamiltonians have been derived and applied to address rotation-torsion-vibration problems. Among others, Pickett [37] proposed an effective Hamiltonian that allows to account for the strong interactions between an in-plane bending and a torsional mode, that is particularly applicable if the torsional barrier is high. This Hamiltonian has also been applied and described in a previous analysis of the pure rotational spectrum of ethyl cyanide carried out by Mehringer et al. [9].

The general form of the rotation-vibration Hamiltonian [37] can be transformed into the commonly used Watson Hamiltonian if the vibrational state is isolated, which is basically the case for the states involved in the CCC deformation and the out-of-plane bending, $v_{12} = 1$ and $v_{20} = 1$, respectively. Here, it is used in the S -reduction. A rotation of the axis system in the ab -plane can be achieved via off-diagonal $D_{ab}(P_a P_b - P_b P_a)$ terms that connect matrix elements of the same vibrational state; a proper choice of the D_{ab} parameter (see Tab. 2) can be useful to decrease the vibrational angular momentum.

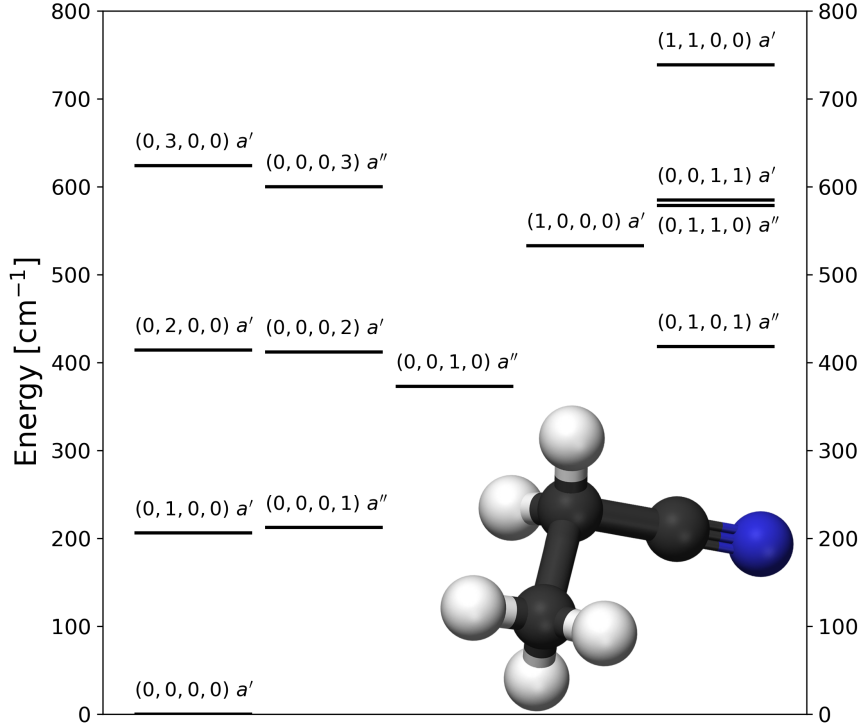


Figure 6: Location and symmetry of the four lowest vibrational states of ethyl cyanide along with nearby combination and overtone states. All states are labelled according to the $(v_{12}, v_{13}, v_{20}, v_{21})$ formalism where the number of quanta of excitation in each state is reported.

It has also been shown that the axis system can be rotated, such that the rotation-torsion Hamiltonian takes the form of a Mathieu equation and its Eigenvalues and Eigenvectors can be expressed as Fourier series related to an expansion in free rotor basis functions (shown also by Groner [38]). In this approach, the rotational parameters are basically multiplied by terms of sine- (S), cosine- (C), or both series, dependent on the symmetry of the operator:

$$C_q = \cos\left(\frac{\pi}{3}q(2\sigma - (K' + K'')\rho)\right) \quad (1)$$

$$S_q = \sin\left(\frac{\pi}{3}q(2\sigma - (K' + K'')\rho)\right) \quad (2)$$

The internal rotation parameter ρ is the ratio of the inverse mass of inertia of the internal rotor F to the inverse mass of the molecular frame, whereas $\sigma = 0, 1, 2$ can be related to the torsional substate ($0 \equiv A; 1, 2 \equiv E$). q is the ordinal number of the Fourier term and K is the projection of the rotational angular momentum. Thus, the torsional

motion is described by additional Fourier constants, tunneling parameters, that have to be included in the set of parameters and that are adjusted in the fit. The series converges rapidly in the high barrier case and usually only very few Fourier constants are necessary. It is important to note that the Fourier constants are rather phenomenological and it is not straightforward to extract quantitative information about the torsional potential. In addition, interactions between different vibrational levels are described by the common off-diagonal matrix elements, such as the Coriolis terms of a and b symmetry applied within this work, that connect here levels between in-plane bend and torsion. In the context of this work, tunneling parameters were included for the excited states $v_{13} = 1$ and $v_{21} = 1$. The excited torsional state $v_{21} = 1$ shows a larger torsional splitting, because its rotational levels are energetically closer to the barrier than those of the other three states. This is also reflected in the size of the tunneling parameters obtained from the combined fit (see Tab. 4), which is discussed in Sec. 4.7.

4. Analysis

4.1. The Automated Spectral Line Assignment Procedure, ASAP

The ASAP software, which was used to assign the spectral features in the ro-vibration spectra, has been described in details in Ref. [22]. Here, we report a brief introduction to the software in its current version, which includes several upgrades compared to the previously reported one. The applicability of ASAP requires that the rotational energy levels within one vibrational state, which is called *reference state* in the following and which is usually the vibrational ground state, are accurately known from a previous analysis. Furthermore, transition frequencies for the rotational-vibrational transitions of interest have to be calculated based on this analysis. The approach is closely related to the idea of closed loops of three transitions (Ritz combination principle). Here, rovibrational transitions that connect different rotational levels of the *reference state* to one common rotational level of another vibrational state, the *target state*, are selected. As these calculated transition frequencies obey exactly the Ritz combination principle, all rovibrational transitions will show the same $\delta\tilde{\nu} = \tilde{\nu}_{obs} - \tilde{\nu}_{calc}$ difference between observed and calculated values, because only the energy of the common *target state* is uncertain whereas the uncertainty of each *reference state* energies is assumed to be negligible.

Shifting the frequency origin of the experimental spectrum ($\tilde{\nu}$) by subtracting the predicted frequency $\tilde{\nu}_{calc}^t$ of any arbitrarily selected transition t moves its peak position from $\tilde{\nu}_{obs}^t$ to the difference frequency $\delta\tilde{\nu}^t$. Thus, transitions are shifted in these scaled spectra $\hat{S}^t(\tilde{\nu}) = S(\tilde{\nu} + \delta\tilde{\nu}^t)$ to the same position if they share a common target state. This position is potentially easy to determine by looking at cross correlation plots. These are obtained by multiplying the intensities of all spectra \hat{S}^t associated with transitions that share a common target state (similarly to the “stacking” procedure, where intensities are summed up). Typically, only one single well-discernible feature (cross-correlation peak) appears in each cross correlation plot as long as the spectral density is relatively low and the spectral features are not too weak. This is nicely seen in the cross correlation plots for S₂O [see Figs. 5 and 6 in Ref. 22]. The offset frequency $\delta\tilde{\nu}$ is then determined from the peak position. The experimental state energy and the frequency can then be derived

as the sum of the calculated state energy / frequency and this offset. Line intensities can vary by orders of magnitude along the transitions. Therefore, weighting the spectral intensities $S(\tilde{\nu} - \tilde{\nu}_{calc})$ has been introduced in the present version of the ASAP software in order to increase the contrast in the cross correlation plots. This is realized by replacing the observed signal in the evaluation by the power of the observed signal with the logarithmic value of the calculated intensity as argument:

$$S_{ccp}(\tilde{\nu}) = \prod_t S^t(\tilde{\nu} + \tilde{\nu}_{calc}^t)^{(\log I_{calc}^t - \log I_{calc}^{min})} \quad (3)$$

where S_{ccp} is the intensity on the cross-correlation plot and I^{min} is the lowest intensity in the set of associated transitions. $\log I_{calc}^t$ and $\log I_{calc}^{min}$ are direct outputs of the SPCAT software, which is part of H. Pickett’s CALPGM suite [39], which was used in the analysis.

4.2. Re-fit of the literature data

In the first step of spectroscopic analysis, the fit of the ground vibrational state of propionitrile as presented in the Cologne Database for Molecular Spectroscopy, CDMS [40, 41], has been reproduced with CALPGM. This fit is based on experimental data from Refs. [1, 11, 12, 42–45]. These data include transitions for the *A* species covering quantum numbers up to $J = 130$ and $K_a = 36$. Frequencies with experimental uncertainties larger than 50 kHz and 100 kHz below and above 500 GHz, respectively, have not been included in the fit (following the CDMS dataset). The data allowed to constrain the energies of the rotational states in the ground vibrational state within this range of quantum numbers accurately enough to apply ASAP. For these states, the energy uncertainty is more than one order of magnitude smaller than the linewidth observed in the IR spectra. The same applies for the torsional splitting, which is small in the ground vibrational state and has only been observed in few transitions. In particular, it is also much smaller than the IR linewidth. Therefore, it has been neglected in the fit and thus also in the calculation of the ground state energy levels. Transition frequencies for *A* and *E* states have been averaged.

4.3. CCN deformation ν_{12} & CCN out-of-plane bend ν_{20}

Cross correlation plots for both ν_{12} and ν_{20} fundamental bands have been calculated using the

500 μ bar experimental spectrum and were based on accurate rotational constants derived from the refit of the literature values for the A symmetry species. Previously published data involving these states [10–12, 45, 46] cover transitions up to $J = 71$, $K_a = 25$ for ν_{20} and $J = 71$, $K_a = 17$ for ν_{12} . Thus, the predicted transition frequencies were already quite accurate and mainly the band center remained to be determined, although interactions as well as the torsional splitting have been neglected. In addition, both bands are intense and well separated (Figs. 1, 2, 3). Only weaker hot bands or combination bands complicate the spectrum in these spectral ranges. Therefore, it was straightforward to localize one peak in each cross correlation plot that is associated with its target state; basically, all peaks appeared within a narrow frequency region (Fig. 7). The offset $\delta\tilde{\nu}$ for each target state, and thus the associated experimental state energies and frequencies, have then been determined for a number of target states, starting with low K_a quantum numbers. In an iterative manner, state energies were assigned and included in the fit in order to improve the predicted frequencies used in the assignment until target states up to $K_a = 25$, $J = 80$ and $K_a = 18$, $J = 80$ for ν_{20} and ν_{12} , respectively, were reached. One avoided crossing has been found in ν_{12} at $K_a = 13$ and $J \approx 49$.

4.4. CCN in-plane bend ν_{13} & Torsion ν_{21}

The energetically lowest fundamental modes ν_{21} and ν_{13} are only separated by a few cm^{-1} . Thus, they appear in the same spectral region and are overlapped significantly (Fig. 1). Strong interactions between these states have been reported previously [9, 15, 36]. Effectively, treating the vibrational states separately becomes impractical and as a result the notation $\nu_{13} + \nu_{21} = 1$ may be used, which accounts for one quantum of excitation in either ν_{13} or ν_{21} . The spectral features turned out to be much stronger than those seen for the two other modes, ν_{20} and ν_{12} , which required to record this spectral range separately and at lower pressure. First, predictions were prepared only for A symmetry species of the ν_{13} mode. The initial fit included frequencies obtained by Fukuyama et al. [15]. Interactions as well as the torsional splittings were neglected. Although a larger number of peaks (false positives) were present in the cross correlation plots of ν_{13} compared to the previous ones, series of cross correlation peaks (true positives) could be determined and allowed to deter-

mine already a large number of state energies that could be included in the fit. In a following step, transitions from Fukuyama et al. [15] for $\nu_{21} = 1$ were included in the analysis. They constrained not only rotational constants for $\nu_{21} = 1$, but provided also some information on the interaction and the energy difference between both vibrational states. Step by step, more and more ν_{13} state energies were assigned. In the subsequent analysis of ν_{21} , the previous determination of first interaction terms, and thereby improved accuracy of predicted frequencies and band center of ν_{21} , was crucial to identify and assign series of cross correlation peaks. As ν_{21} transitions are weaker than those from the other band, the cross correlation plots for ν_{21} show many more peaks (false positives) caused by strong transitions in this spectral region that are not well enough suppressed by the multiplication process (Fig. 7). Nevertheless, the assignment of ν_{21} state energies was possible, because the cross correlation peaks (true positives) could be localized within a narrow spectral window of only a few tenths of a wavenumber. Again, higher J , K_a levels were assigned and stepwise refined the predictions. In general, assignments for ν_{21} are less secure compared to those for the other bands, because the identification of cross correlation peaks is ambiguous in a number of cases. This can also be seen in the cross correlation plots (Fig. 7) for the series of target states with $K_a = 10$, $K_c = J - K_a$.

4.5. Wavenumber accuracy of the ro-vibrational lines

Energy levels obtained via ASAP have been used to calculate frequencies for pure rotational transitions within vibrationally excited states that either were previously reported [10, 15] or observed within this work. By comparison with accurate values observed with millimeter-wave techniques, the accuracy of state energies derived from IR spectra using ASAP was estimated. Fig. 8 shows the probability density of frequency differences calculated for each vibrational state. Standard deviations between $\sigma = 4.4 \text{ MHz}$ ($\sim 0.00015 \text{ cm}^{-1}$) and $\sigma = 11.9 \text{ MHz}$ ($\sim 0.0004 \text{ cm}^{-1}$) were determined from the data assuming a normal distribution. By taking the largest value and weighting it with a $\sqrt{0.5}$ factor, because the energy differences are calculated from two experimental values, the accuracy of ASAP-derived state energies should at least be better than 0.0003 cm^{-1} . Also, it is worth

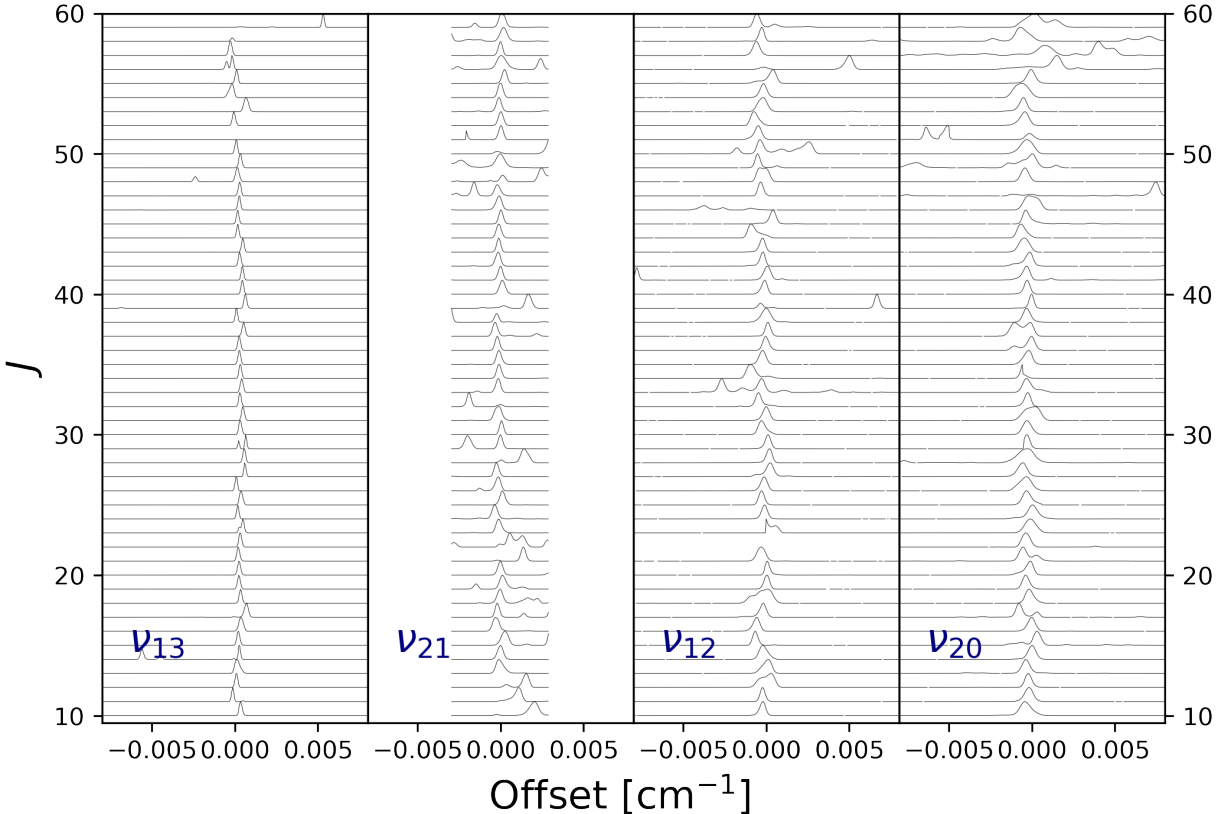


Figure 7: Cross correlation plots for $K_a = 10$, $K_c = J - K_a$ for the fundamental modes ν_{13} , ν_{21} , ν_{12} , and ν_{20} . Intensities are normalized with respect to the strongest peak in the displayed spectral range. A larger number of transitions included in the cross correlation plots leads to a narrowing of peaks, which can be seen clearly in the plots for ν_{13} .

noting that the mean frequency difference is below 500 kHz ($\sim 0.00002 \text{ cm}^{-1}$) in all cases. The smaller standard deviation obtained for ν_{13} results from a larger number of observed transitions that contribute to each individual cross correlation plot and thus cause a narrowing of the cross correlation peak. This can also be seen in the cross correlation plots of ν_{13} shown in Fig. 7. Overall, the comparison confirms that the frequency accuracy in the IR data is better than the assigned uncertainty of 0.0005 cm^{-1} . Nevertheless, a slightly higher uncertainty is assigned, because uncertainties of the vibrational ground state energies are not taken into account in this comparison.

4.6. Pure rotational spectra within $\nu_{13} + \nu_{21} = 1$

A substantial number of pure rotational transitions within the excited states $\nu_{13} + \nu_{21} = 1$ have been assigned in the millimeter-wave spectra

recorded in Cologne (see Fig. 5), although a comprehensive analysis of the rotational spectrum is beyond the scope of this paper. Here, the main goal was to evaluate if predictions derived from the IR study help to facilitate substantially the assignments and could already support astronomical line identifications. It turned out that line positions were generally well predicted and transitions involving K_a quantum numbers above 10 could easily be assigned. Nevertheless, the torsional splitting, observed not only for transitions in $\nu_{21} = 1$, but also for many in $\nu_{13} = 1$, had to be taken into account. Thus, torsional parameters had to be included in the fit, whose values were constrained by frequencies reported for the E -symmetry species by Fukuyama et al. [15]. In the following, transitions were assigned in the millimeter-wave spectrum in the usual stepwise manner, starting from low to

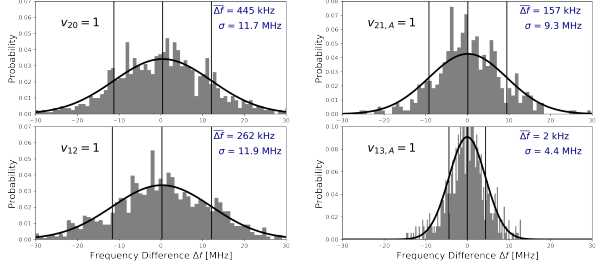


Figure 8: Probability density of frequency differences for pure rotational transitions determined between observed frequencies of $\text{C}_2\text{H}_5\text{CN}$ (Refs. [10, 15] and this work) and calculated ones derived from the state energies derived using ASAP. The different plots show values for each of the vibrational states studied in this work. Only A symmetry states are taken into account.

high J and K_a quantum numbers.

4.7. Combined effective fit

In total, 13473 energy offsets and additional 1292 distinct pure rotational transition frequencies were determined and assigned to 86063 and 1813 transitions, respectively. Energy levels up to $K_a = 25$ and $J = 90$ were accessed. A summary of the experimental dataset is given Tab. 1. Line accuracies of 0.0005 cm^{-1} were assigned to state energies and IR transitions while for the pure rotational transitions they were individually estimated with regard of the fit of the line profiles and take typical values of 50 kHz for isolated lines and 100 kHz for blended ones. Previously reported lines were treated with their reported uncertainty. 331 of these frequencies ($v_{12} = 1$ and $v_{20} = 1$) were not included, because assigned and calculated position deviated by more than four times their uncertainty, most likely, caused by perturbations with higher energy levels (see Fig. 6). State energies rather than transition wavenumbers were included in the experimental dataset derived via ASAP (as discussed in Ref. [22]). The state energies are coded in SPFIT as transitions from the lowest level in the vibrational ground state ($J_{K_a, K_c} = 0_{0,0}, v = 0$) to the corresponding target state.

At first, parameters of an asymmetric rotor Hamiltonian in Watson's S reduction were used to reproduce frequencies of previously published rotational transitions and the newly assigned rovibrational transitions for the A symmetry species. Be-

sides the state energy, only the parameters that led to an improvement of the fit were released. Otherwise their value was fixed to the corresponding value obtained for the vibrational ground state. Coriolis coupling terms with a - and b -symmetry were included to describe the strong interactions that are observed between the torsion and the in-plane-bending vibrational state. The importance of individual coupling terms has been judged based on the achieved improvement of the fit. This led to an extensive set of parameters. A qualitative and more detailed analysis of the single interaction terms is beyond the scope of this work and will be carried out later in combination with a comprehensive study of the pure rotational spectra. The far better accuracy achieved at millimeter-wavelengths will provide superior constraints to these parameters.

In a second step, transitions within the E symmetric substates of the torsion and the in-plane bend were also taken into account. In this phenomenological approach (see section 3), the description of the internal rotation is achieved by expanding the energy and the rotational terms of each vibrational state into Fourier series. Here, only the internal rotation parameter ρ and the first cosine term for the energy with its coefficient ϵ_1 , and for the rotational operators $P^2, P_z^2, P_+^2 - P_-^2$ with their coefficients T_1^{001}, T_1^{010} , and T_1^{100} , were included for the torsionally excited states. The observed splitting of transitions within the in-plane bend was already reasonably described by the strong mixing of levels with torsional states. Nevertheless, adding ϵ_1 also for the in-plane bend, improved the fit noticeably.

Details about the coding of these parameters in SPFIT are given by Drouin [47]. The splitting that was observed by Fukuyama et al. [15] for some b -type transitions of the out-of-plane bending vibrational state $v_{20} = 1$ has been neglected and only frequencies reported for the A symmetry species have been included in the fit. SPFIT does not allow to determine the internal rotation parameter ρ in the fit. Thus, its initial value was calculated using the structural information reported by Heise et al. [48] and moments of inertia derived from the rotational constants. Later on, ρ was manually adjusted to better reproduce the observed transition frequencies. Changing the value of ρ in steps of 0.001 within a range of about ± 0.01 has only little impact on the final rms value and only values beyond this range considerably worsen the fit.

Tabs. 2, 4, 3 and 5 show the final set of parameters that were obtained from the combined fit. A common problem in the spectral analysis of molecules with internal rotation is the state labeling by asymmetric top quantum numbers, because it depends on the diagonalization and energy ordering. Thus, the assigned asymmetric top quanta might change for a small subset of states during the fitting process, in particular if the asymmetric splitting is of the same magnitude as the torsional splitting. Therefore, all lines that deviate by more than 20σ , i.e. 145 out of 13618 state energies, were rejected from the fit. Also, 14 pure rotational transitions are not reproduced within this limit and are rejected from the fit. ν_{12} transitions that involve $K_a = 13$ states were not included. These levels are probably perturbed by one of the nearby vibrational states $\nu_{20} + \nu_{13}$ or $\nu_{20} + \nu_{21}$. The final fit reproduces the experimental dataset with almost experimental uncertainty with unitless, weighted standard deviation of 1.46. The standard deviation is considerably different between IR and microwave data sets, because deficiencies of the model are more significant for the microwave data with its much higher absolute accuracy. The standard deviation for each individual dataset is included in Tab. 1.

Transition frequencies and intensities have been calculated with SPCAT based on the current analysis and used to simulate all four fundamental bands (Figs. 2,3,4) and the rotational spectrum at millimeter-wavelength (Fig. 5). The very good agreement between simulation and experiment shows the quality of the predictions and validates also the overall correctness of assignments done with ASAP. Partition functions have been calculated based on the summation of energies. All states investigated in this work ($v = 0$, $\nu_{12} = 1$, $\nu_{13} = 1$, $\nu_{20} = 1$, $\nu_{21} = 1$) and energy levels up to $J = 150$ and $K_a = 70$ have been taken into account. A listing of the experimental dataset and partition functions will be given in the supplementary material in electronic form. Predictions will also be provided via CDMS.

5. Astronomical observation of vibrational satellites

Ethyl cyanide has been detected in several astronomical sources in the last years [see e.g., 49, 50], and it is expected to be abundant in star-forming regions where newly-born stars heat up their surroundings and release large amounts of complex or-

ganic species from grain surfaces into the gas phase. Once in the gas phase, these species are detectable with telescope facilities operating in the millimeter and sub-millimeter regimes such as the Atacama Large Millimeter/submillimeter Array [ALMA; 51].

We have studied the high-mass star-forming complex G327.3–0.6 (hereafter G327) with ALMA during its Cycle 4 (project code 2016.1.00168.S). G327, with a luminosity of $\sim 2 \times 10^5 L_\odot$ and at a distance of 3.3 kpc [52], is best known as one of the brightest and chemically richest hot molecular cores in our vicinity [see e.g., 53–55]. Our ALMA observations have imaged the region where the hot molecular core G327 is located at an angular resolution of 1''.4 (corresponding to ≈ 4500 au) and in different frequency ranges across the ALMA band 6 (211–275 GHz). In Fig. 9 (see black line), we present a spectrum extracted towards G327 in three frequency ranges.

The spectrum towards G327 is rich in many spectral line features. We have modeled it using the software XCLASS [eXtended CASA Line Analysis Software Suite; 56], which makes use of the Cologne Database for Molecular Spectroscopy [CDMS; 40, 57] and Jet Propulsion Laboratory [JPL; 58] catalogs, via the Virtual Atomic and Molecular Data Centre [VAMDC; 41]. In the synthetic spectrum (see inverted grey line in Fig. 9), we have considered more than 23 different molecular species (excluding isotopologues and excited states; Zhang et al., in prep.). A number of bright and isolated spectral lines remained unidentified in the synthetic spectrum (e.g., at frequencies 216.05, 216.55, 217.95 GHz). Most of these unidentified features are now assigned to vibrationally excited C_2H_5CN ($\nu_{13} + \nu_{21} = 1$) transitions measured in this work (cf. blue line in Fig. 9). We derive a C_2H_5CN column density of $9.5 \times 10^{17} \text{ cm}^{-2}$ with a temperature of 250 K. This column density and temperature are comparable to the values derived for other commonly-studied species such as CH_3OH ($1.8 \times 10^{19} \text{ cm}^{-2}$, 260 K) CH_3OCHO ($3.4 \times 10^{18} \text{ cm}^{-2}$, 270 K), CH_3COCH_3 ($1.1 \times 10^{18} \text{ cm}^{-2}$, 170 K), HC_3N ($5.0 \times 10^{17} \text{ cm}^{-2}$, 235 K), $HNCO$ ($3.9 \times 10^{17} \text{ cm}^{-2}$, 290 K). Comparison between C_2H_5CN ground and vibrationally-excited states can be used to obtain information on the temperature and density structure of G327 (Zhang et al., in prep.). Furthermore, given the bright detections of the $\nu_{13} + \nu_{21} = 1$ transitions, we expect other vibrationally excited states (e.g., $\nu_{13} + \nu_{21} = 2$) to be equally bright. Further laboratory measurements

involving these excited states will be key to better characterize and understand the structure of astronomical sources such as star-forming regions.

6. Conclusions and prospects

The high resolution infrared spectrum of ethyl cyanide, $\text{C}_2\text{H}_5\text{CN}$, a prototypical saturated organic nitrile abundantly found in the interstellar medium, has been studied for the first time. The four lowest fundamental vibrational modes of ethyl cyanide have been measured on the AILES beamline of the SOLEIL synchrotron facility, and analyzed allowing the derivation of highly accurate vibrational state energies. The Automated Spectral Assignment Procedure, ASAP, has been improved and demonstrated once more to be a very useful analysis tool greatly simplifying the line assignment even of rather dense rotational-vibrational spectra.

Some limitations of ASAP became evident in the analysis of the fundamental torsional band ν_{21} , where the identification of cross correlation peaks was hampered by severe spectral congestion. Nevertheless, this band along with the close-by lying and strongly interacting CCN-bending mode ν_{13} could finally be disentangled. Based on the available molecular parameters for the ν_{20} and ν_{12} states from previous millimeter-/submillimeter-wave studies, the ASAP treatment of the corresponding vibrational fundamentals was accomplished in a rather straightforward fashion. Subsequent pure rotational measurements within the ground state and the four lowest vibrationally excited states have supported further refinement of the spectroscopic constants.

Although an even more comprehensive and detailed analysis of the millimeter- and submillimeter wave spectra within these excited states is still highly desirable, the current quality of predicted rest frequencies has already proven very reliable for the interpretation of astronomical spectra. The ALMA spectrum recorded towards the high-mass star-forming region G327.3–0.6, demonstrates the very favorable agreement between the predicted frequencies and the astronomical observations. The very strong spectral features related to transitions within excited vibrational states also shows their importance for the interpretation of astronomical spectra. Given the intensity of the vibrational satellites observed towards G327.3–0.6 it seems likely that vibrational satellites from energetically higher lying vibrational states might

also be detected once their laboratory millimeter-/submillimeter-wave spectra are known to sufficient accuracy. Besides satellites from the ν_{20} and ν_{12} states also studied here, future investigations of overtones and combination modes of ν_{13} and ν_{21} seem indicated, as seem studies of the combination modes of ν_{13} and ν_{21} with either ν_{20} and ν_{12} . Close inspection of the vibrational fundamentals observed here already reveal some weak signatures that may hint towards the presence of hot bands, however, no attempt has been made here towards their analysis. Also, spectroscopic studies of vibrational modes above 600 cm^{-1} followed by spectroscopic analysis using ASAP should be feasible.

In the future, comprehensive infrared laboratory studies of vibrational bands of complex organic species followed by sophisticated spectroscopic analyses with the help of ASAP turns into a very promising avenue towards understanding their vibrational satellite pure rotational spectra. This strategy should be applicable to many astronomical species known to contribute substantially to the rich emission features observed towards line-rich astronomical sources.

After completion of the present manuscript, right before submission, we learned about a manuscript by Zbigniew Kisiel and collaborators just accepted to the Journal of Molecular Spectroscopy [59]. In their study, the authors investigated the pure rotational spectrum of ethyl cyanide in the $v_{13} + v_{21} = 1$ states employing millimeter wave measurements and present a new global fit. Since the models used in their and in our study are not strictly identical, quantitative agreement cannot be expected. However, qualitatively, the two parameters sets seem in reasonable accord. For example, the energy difference between ν_{21} and ν_{13} derived in their millimeter wave study is $6.2070246(14) \text{ cm}^{-1}$ compared to a value of $6.207002(25) \text{ cm}^{-1}$ derived here from the vibrational band centers of the A states. Also, the leading Coriolis type interaction parameters G_a and G_b compare well and agree to within some 4% (G_a) and 18% (G_b). Future predictions should benefit from one unified model comprising both new datasets.

Acknowledgement

We acknowledge the SOLEIL facility for provision of synchrotron radiation under the proposals 20170138 & 20190316. This work has

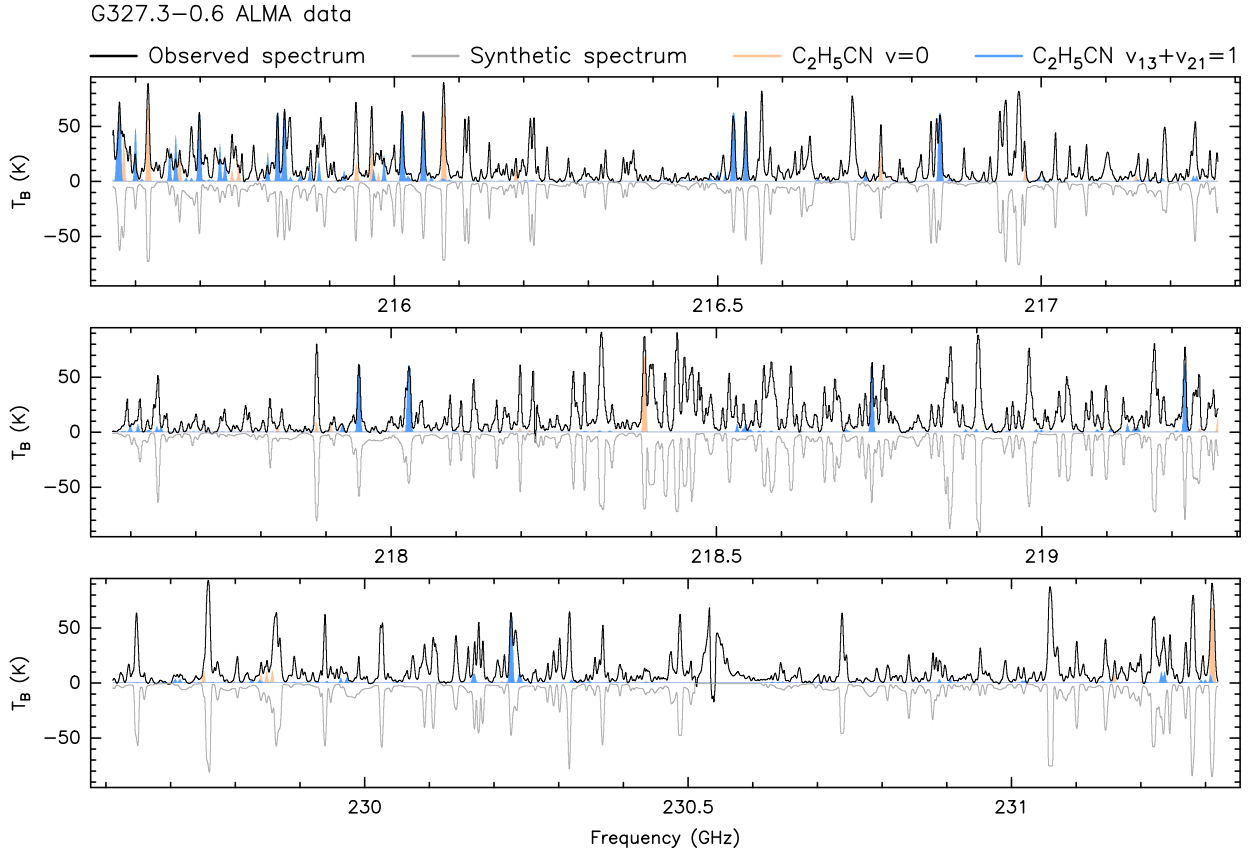


Figure 9: Spectra towards the high-mass star-forming region G327.3–0.6, with the intensity in brightness temperature unit (T_B). ALMA observational data in black. Synthetic spectrum including all identified molecular species (see Sect. 5) in grey, and with the intensity multiplied by a factor -1 . The contribution from $C_2H_5CN\,v = 0$ and $C_2H_5CN\,v_{13} + v_{21} = 1$ transitions are highlighted in orange and blue, respectively.

been supported via Collaborative Research Centre 956, sub-projects B3 and A6, funded by the Deutsche Forschungsgemeinschaft (DFG; project ID 184018867) and DFG SCHL 341/15-1 (“Cologne Center for Terahertz Spectroscopy”). The work in Cambridge is supported from NASA grant 80NSSC18K0396. We thank Holger S. P. Müller for helpful discussions.

Appendix: Supplementary data

Supplementary data associated with this article (parameter and fit files) are available on ScienceDirect (www.sciencedirect.com).

References

- [1] D. Johnson, F. Lovas, C. Gottlieb, E. Gottlieb, M. Litvak, M. Guelin, P. Thaddeus, Detection of interstel-

lar ethyl cyanide, *Astrophys. J.* **218** (1977) 370–376. doi:10.1086/155691.

- [2] S. Cazaux, A. G. G. M. Tielens, C. Ceccarelli, A. Castets, V. Wakelam, E. Caux, B. Parise, D. Teyssier, The Hot Core around the Low-Mass Protostar IRAS 16293-2422: Scoundrels Rule!, *Astrophys. J.* **593** (2003) L51–L55.
- [3] K. Demyk, H. Mäder, B. Tercero, J. Cernicharo, J. Demaison, L. Margulès, M. Wegner, S. Keipert, M. Sheng, Isotopic ethyl cyanide $^{13}CH_3CH_2CN$, $CH_3^{13}CH_2CN$, and $CH_3CH_2^{13}CN$: laboratory rotational spectrum and detection in Orion, *Astron. Astrophys.* **466** (2007) 255–259.
- [4] H. S. P. Müller, A. Belloche, K. M. Menten, C. Comito, P. Schilke, Rotational spectroscopy of isotopic vinyl cyanide, $H_2C=H-C\equiv N$, in the laboratory and in space, *J. Mol. Spectrosc.* **251** (2008) 319–325.
- [5] L. Margulès, R. Motiyenko, K. Demyk, B. Tercero, J. Cernicharo, M. Sheng, M. Weidmann, J. Gripp, H. Mäder, J. Demaison, Rotational spectrum of deuterated and ^{15}N ethyl cyanides: CH_3CHDCN and CH_2DCH_2CN and of $CH_3CH_2C^{15}N$, *Astron. Astro-*

- phys. 493 (2009) 565–569.
- [6] L. Margulès, A. Belloche, H. S. P. Müller, R. A. Motiyenko, J. C. Guillemin, R. T. Garrod, K. M. Menten, Spectroscopic study and astronomical detection of doubly ^{13}C -substituted ethyl cyanide, *Astron. Astrophys.* 590 (2016) A93.
- [7] A. Belloche, H. S. P. Müller, R. T. Garrod, K. M. Menten, Exploring molecular complexity with ALMA (EMoCA): Deuterated complex organic molecules in Sagittarius B2(N2), *Astron. Astrophys.* 587 (2016) A91.
- [8] E. Gibb, A. Nummelin, W. M. Irvine, D. C. B. Whitet, P. Bergman, Chemistry of the Organic-Rich Hot Core G327.3-0.6, *Astrophys. J.* 545 (2000) 309–326. doi:10.1086/317805.
- [9] D. M. Mehringer, J. C. Pearson, J. Keene, T. G. Phillips, Detection of vibrationally excited Ethyl Cyanide in the Interstellar Medium, *Astrophys. J.* 608 (2004) 306–313. doi:10.1086/386357.
- [10] A. M. Daly, C. Bermúdez, A. López, B. Tercero, J. C. Pearson, N. Marcelino, J. L. Alonso, J. Cerñicharo, Laboratory Characterization and Astrophysical Detection of vibrationally excited States of Ethyl Cyanide, *Astrophys. J.* 768 (2013) 81. doi:10.1088/0004-637X/768/1/81.
- [11] J. C. Pearson, K. V. L. N. Sastry, E. Herbst, F. C. de Lucia, The submillimeter-wave spectrum of propionitrile ($\text{C}_2\text{H}_5\text{CN}$), *Astrophys. J. Suppl. S.* 93 (1994) 589. doi:10.1086/192069.
- [12] C. S. Brauer, J. C. Pearson, B. J. Drouin, S. Yu, New Ground-State Measurements of Ethyl Cyanide, *Astrophys. J. Suppl. S.* 184 (2009) 133–137. doi:10.1088/0067-0049/184/1/133.
- [13] S. M. Fortman, I. R. Medvedev, C. F. Neese, F. C. De Lucia, A new approach to astrophysical spectra: The complete experimental spectrum of ethyl cyanide ($\text{CH}_3\text{CH}_2\text{CN}$) between 570 and 645 GHz, *Astrophys. J.* 714 (2010) 476–486.
- [14] F. J. Lovas, Microwave Spectra of Molecules of Astrophysical Interest. XXI. Ethanol ($\text{C}_2\text{H}_5\text{OH}$) and Propionitrile ($\text{C}_2\text{H}_5\text{CN}$), *J. Phys. Chem. Ref. Data* 11 (1982) 251–312.
- [15] Y. Fukuyama, K. Omori, H. Odashima, K. Takagi, S. Tsunekawa, Analysis of Rotational Transitions in Excited Vibrational States of Propionitrile ($\text{C}_2\text{H}_5\text{CN}$), *J. Mol. Spectrosc.* 193 (1999) 72–103. doi:10.1006/jmsp.1998.7730.
- [16] A. O. Pienkina, L. Margulès, R. A. Motiyenko, H. S. P. Müller, J. C. Guillemin, The millimeter and submillimeter rotational spectrum of triple ^{13}C -substituted ethyl cyanide, *Astron. Astrophys.* 601 (2017) A2.
- [17] N. E. Duncan, G. J. Janz, Molecular Structure and Vibrational Spectra of Ethyl Cyanide, *J. Chem. Phys.* 23 (1955) 434–440.
- [18] W. E. Wurrey, B. J. R., C. J. Durig, Vibrational spectra and normal coordinate analysis of ethyl cyanides, *J. Phys. Chem.* 80 (1976) 1129–1136.
- [19] H. M. Heise, F. Winther, H. Lutz, The Vibrational-Spectra of Some Isotopic-Species of Propionitrile, *J. Mol. Spectrosc.* 90 (1981) 531–571.
- [20] F. Cerceau, F. Raulin, R. Courtin, D. Gautier, Infrared-Spectra of Gaseous Mononitriles - Application to the Atmosphere of Titan, *Icarus* 62 (1985) 207–220.
- [21] A. Toumi, N. Piétri, I. Couturier-Tamburelli, Infrared study of matrix-isolated ethyl cyanide: simulation of the photochemistry in the atmosphere of Titan, *Phys. Chem. Chem. Phys.* 17 (2015) 30352–30363.
- [22] M. A. Martin-Drumel, C. P. Endres, O. Zingsheim, T. Salomon, S. Thorwirth, The SOLEIL view on sulfur rich oxides: The S_2O bending mode at 380 cm^{-1} and its analysis using an Automated Spectral Assignment Procedure (ASAP), *J. Mol. Spectrosc.* 315 (2015) 72–79. doi:10.1016/j.jms.2015.02.014.
- [23] S. Thorwirth, M. A. Martin-Drumel, C. P. Endres, T. Salomon, O. Zingsheim, J. van Wijngaarden, O. Pirali, S. Gruet, F. Lewen, S. Schlemmer, M. C. McCarthy, An ASAP treatment of vibrationally excited S_2O : The ν_3 mode and the $\nu_3 + \nu_2 - \nu_2$ hot band, *J. Mol. Spectrosc.* 319 (2016) 47–49.
- [24] M.-A. Martin-Drumel, J. P. Porterfield, M. Goubet, P. Asselin, R. Georges, P. Soulard, M. Nava, P. B. Changala, B. E. Billinghamurst, O. Pirali, M. C. McCarthy, J. H. Baraban, Synchrotron-Based High Resolution Far-Infrared Spectroscopy of trans-Butadiene, *J. Phys. Chem. A* 124 (2020) 2427–2435.
- [25] J.-B. Brubach, L. Manceron, M. Rouzières, O. Pirali, D. Balcon, F. Kwabia-Tchana, V. Boudon, M. Tudorie, T. Huet, A. Cuisset, P. Roy, Performance of the AILES THz-Infrared beamline at SOLEIL for High resolution spectroscopy, in: *WIRMS 2009*, volume 1214 of *AIP Conference Proceedings*, 2010, pp. 81–84.
- [26] O. Pirali, V. Boudon, J. Oomens, M. Vervloet, Rotationally resolved infrared spectroscopy of adamantane, *J. Chem. Phys.* 136 (2012) 024310.
- [27] O. Pirali, M. Goubet, T. R. Huet, R. Georges, P. Soulard, P. Asselin, J. Courbe, P. Roy, M. Vervloet, The far infrared spectrum of naphthalene characterized by high resolution synchrotron FTIR spectroscopy and anharmonic DFT calculations, *Phys. Chem. Chem. Phys.* 15 (2013) 10141–10150. doi:10.1039/c3cp44305a.
- [28] V.-M. Horneman, R. Anttila, S. Alanko, J. Pietilä, Transferring calibration from CO_2 laser lines to far infrared water lines with the aid of the ν_2 band of OCS and the ν_2 , $\nu_1-\nu_2$, and $\nu_1+\nu_2$ bands of $^{13}\text{CS}_2$: Molecular constants of $^{13}\text{CS}_2$, *J. Mol. Spectrosc.* 234 (2005) 238–254. doi:10.1016/j.jms.2005.09.011.
- [29] F. Matsushima, H. Odashima, T. Iwasaki, S. Tsunekawa, K. Takagi, Frequency measurement of pure rotational transitions of H_2O from 0.5 to 5 THz, *Journal of Molecular Structure* 352–353 (1995) 371–378. doi:10.1016/0022-2860(94)08531-1.
- [30] F. Matsushima, N. Tomatsu, T. Nagai, Y. Moriwaki, K. Takagi, Frequency measurement of pure rotational transitions in the $\nu_2 = 1$ state of H_2O , *J. Mol. Spectrosc.* 235 (2006) 190–195. doi:10.1016/j.jms.2005.11.003.
- [31] I. E. Gordon, L. S. Rothman, C. Hill, R. V. Kochanov, Y. Tan, P. F. Bernath, M. Birk, V. Boudon, A. Campargue, K. Chance, et al., The HITRAN2016 molecular spectroscopic database, *J. Quant. Spectrosc. Rad. Transfer* 203 (2017) 3–69.
- [32] M. A. Martin-Drumel, J. van Wijngaarden, O. Zingsheim, F. Lewen, S. Thorwirth, Millimeter- and submillimeter-wave spectroscopy of disulfur dioxide, OSSO, *J. Mol. Spectrosc.* 307 (2015) 33–39. doi:10.1016/j.jms.2014.11.007.
- [33] M. H. Ordu, O. Zingsheim, A. Belloche, F. Lewen, R. T. Garrod, K. M. Menten, S. Schlemmer, H. S. P. Müller, Laboratory rotational spectroscopy of isotopic acetone, $\text{CH}_3\text{C}(^{13}\text{C})\text{CH}_3$ and $^{13}\text{CH}_3\text{C}(\text{O})\text{CH}_3$, and astronomical search in Sagittarius B2(N2), *Astron. Astrophys.*

- 629 (2019) A72. doi:10.1051/0004-6361/201935887.
- [34] A. Kraśnicki, Z. Kisiel, Electric dipole moments of acrylonitrile and of propionitrile measured in supersonic expansion, *J. Mol. Spectrosc.* 270 (2011) 83–87. URL: <http://dx.doi.org/10.1016/j.jms.2011.08.006>.
- [35] J. Demaison, L. Margulès, H. Mader, M. Sheng, H. D. Rudolph, Torsional barrier and equilibrium structure of ethyl cyanide, *J. Mol. Spectrosc.* 252 (2008) 169–175.
- [36] C. S. Brauer, J. C. Pearson, B. J. Drouin, S. Yu, Analysis of the Lowest In-Plane Bend and First Excited Torsional State of $\text{CH}_3\text{CH}_2\text{CN}$, in: 64th International Symposium On Molecular Spectroscopy, volume 64, 2009, p. TC07”.
- [37] H. M. Pickett, Theoretical studies of internal rotation for an asymmetric top, *J. Chem. Phys.* 107 (1997) 6732–6735. doi:10.1063/1.474916.
- [38] P. Groner, Large-amplitude motion tunneling parameters in effective rotational Hamiltonians from rotation-internal rotation theory, *J. Mol. Spectrosc.* 156 (1992) 164–189. doi:10.1016/0022-2852(92)90101-S.
- [39] H. M. Pickett, R. L. Poynter, E. A. Cohen, M. L. Delitsky, J. C. Pearson, H. S. P. Müller, Submillimeter, millimeter, and microwave spectral line catalog, *J. Quant. Spectrosc. Radiat. Transfer* 60 (1998) 883–890. doi:10.1016/S0022-4073(98)00091-0.
- [40] H. S. P. Müller, S. Thorwirth, D. A. Roth, G. Winnweisser, The Cologne Database for Molecular Spectroscopy, CDMS, *Astronom. Astrophys.* 370 (2001) L49–L52. doi:10.1051/0004-6361:20010367.
- [41] C. P. Endres, S. Schlemmer, P. Schilke, J. Stutzki, H. S. P. Müller, The Cologne Database for Molecular Spectroscopy, CDMS, in: The Virtual Atomic and Molecular Data Centre, VAMDC, *J. Mol. Spectrosc.* 327 (2016) 95–104. doi:10.1016/j.jms.2016.03.005.
- [42] H. Mäder, H. M. Heise, H. Dreizler, Microwave Spectrum of Ethyl Cyanide; r_0 -Structure, Nitrogen Quadrupole Coupling Constants and Rotation-Torsion-Vibration Interaction, *Zeitschrift für Naturforschung A* 29 (1974). doi:10.1515/zna-1974-0119.
- [43] J. Burie, J. Demaison, A. Dubrulle, D. Boucher, Microwave spectrum of propionitrile: Determination of the quartic and sextic centrifugal distortion constants, *J. Mol. Spectrosc.* 72 (1978) 275–281.
- [44] D. Boucher, A. Dubrulle, J. Demaison, H. Dreizler, Determination of a High Potential Barrier Hindering Internal Rotation from the Analysis of the Ground State Spectrum: The Case of Ethyl Cyanide, *Zeitschrift für Naturforschung A* 35 (1980) 1136–1141.
- [45] Y. Fukuyama, H. Odashima, K. Takagi, S. Tsunekawa, The Microwave Spectrum of Propionitrile ($\text{C}_2\text{H}_5\text{CN}$) in the Frequency Range from 8 to 200 GHz, *Astrophys. J. Suppl. S.* 104 (1996) 329. doi:10.1086/192303.
- [46] S. M. Fortman, I. R. Medvedev, C. F. Neese, F. C. De Lucia, How Complete are Astrophysical Catalogs for the Millimeter and Submillimeter Spectral Region?, *Astrophys. J. Lett.* 725 (2010) L11–L14. doi:10.1088/2041-8205/725/1/L11.
- [47] B. J. Drouin, Practical uses of SPFIT, *J. Mol. Spectrosc.* 340 (2017) 1–15. doi:10.1016/j.jms.2017.07.009.
- [48] H. Heise, H. Mäder, H. Dreizler, Rotation-Torsion-Vibration Interaction in the Rotational Spectra of Isotopic Species of Ethyl Cyanide, *Zeitschrift für Naturforschung A* 31 (1976) 1228–1241. doi:10.1515/zna-1976-1015.
- [49] A. Belloche, R. T. Garrod, H. S. P. Müller, K. M. Menten, C. Comito, P. Schilke, Increased complexity in interstellar chemistry: detection and chemical modeling of ethyl formate and n-propyl cyanide in Sagittarius B2(N), *Astronom. Astrophys.* 499 (2009) 215–232. doi:10.1051/0004-6361/200811550.
- [50] A. Belloche, H. S. P. Müller, K. M. Menten, P. Schilke, C. Comito, Complex organic molecules in the interstellar medium: IRAM 30 m line survey of Sagittarius B2(N) and (M), *Astronom. Astrophys.* 559 (2013) A47. doi:10.1051/0004-6361/201321096.
- [51] ALMA Partnership, E. B. Fomalont, C. Vlahakis, S. Corder, A. Remijan, D. Barkats, R. Lucas, T. R. Hunter, C. L. Brogan, Y. Asaki, S. Matsushita, W. R. F. Dent, R. E. Hills, N. Phillips, A. M. S. Richards, P. Cox, R. Amestica, D. Broguiere, W. Cotton, A. S. Hales, R. Hirhart, A. Hirota, J. A. Hodge, C. M. V. Impellizzeri, J. Kern, R. Kneissl, E. Liuzzo, N. Marcelino, R. Marson, A. Mignano, K. Nakanishi, B. Nikolic, J. E. Perez, L. M. Pérez, I. Toledo, R. Aladro, B. Butler, J. Cortes, P. Cortes, V. Dhawan, J. Di Francesco, D. Espada, F. Galarza, D. Garcia-Appadoo, L. Guzman-Ramirez, E. M. Humphreys, T. Jung, S. Kameno, R. A. Laing, S. Leon, J. Mangum, G. Marconi, H. Nagai, L. A. Nyman, M. Radiszcz, J. A. Rodón, T. Sawada, S. Takahashi, R. P. J. Tilanus, T. van Kempen, B. Vila Vilari, L. C. Watson, T. Wiklund, F. Gueth, K. Tatematsu, A. Wootten, A. Castro-Carrizo, E. Chapillon, G. Dumas, I. de Gregorio-Monsalvo, H. Francke, J. Gallardo, J. Garcia, S. Gonzalez, J. E. Hibbard, T. Hill, T. Kaminski, A. Karim, M. Krips, Y. Kurono, C. Lopez, S. Martin, L. Maud, F. Morales, V. Pietu, K. Plarre, G. Schieven, L. Testi, L. Videla, E. Villard, N. Whyborn, M. A. Zwaan, F. Alves, P. Andreani, A. Avison, M. Barta, F. Bedosti, G. J. Bendo, F. Bertoldi, M. Bethermin, A. Biggs, J. Boissier, J. Brand, S. Burkutean, V. Casasola, J. Conway, L. Cortese, B. Dabrowski, T. A. Davis, M. Diaz Trigo, F. Fontani, R. Franco-Hernandez, G. Fuller, R. Galvan Madrid, A. Giannetti, A. Ginsburg, S. F. Graves, E. Hatziminaoglou, M. Hogerheijde, P. Jachym, I. Jimenez Serra, M. Karlicky, P. Klaasen, M. Kraus, D. Kunneriath, C. Lagos, S. Longmore, S. Leurini, M. Maercker, B. Magnelli, I. Marti Vidal, M. Massardi, A. Maury, S. Muehle, S. Muller, T. Muxlow, E. O’Gorman, R. Paladino, D. Petry, J. E. Pineda, S. Randall, J. S. Richer, A. Rossetti, A. Rushton, K. Rygl, A. Sanchez Monge, R. Schaaf, P. Schilke, T. Stanke, M. Schmalzl, F. Stoehr, S. Urban, E. van Kampen, W. Vlemmings, K. Wang, W. Wild, Y. Yang, S. Iguchi, T. Hasegawa, M. Saito, J. Inatani, N. Mizuno, S. Asayama, G. Kosugi, K. I. Morita, K. Chiba, S. Kawashima, S. K. Okumura, N. Ohashi, R. Ogasawara, S. Sakamoto, T. Noguchi, Y. D. Huang, S. Y. Liu, F. Kemper, P. M. Koch, M. T. Chen, Y. Chikada, M. Hiramatsu, D. Iono, M. Shimojo, S. Komugi, J. Kim, A. R. Lyo, E. Muller, C. Herrera, R. E. Miura, J. Ueda, J. Chibueze, Y. N. Su, A. Trejo-Cruz, K. S. Wang, H. Kiuchi, N. Ukita, M. Sugimoto, R. Kawabe, M. Hayashi, S. Miyama, P. T. P. Ho, N. Kaifu, M. Ishiguro, A. J. Beasley, S. Bhatnagar, I. Braatz, J. A., D. G. Brisbin, N. Brunetti, C. Carilli, J. H. Crossley, L. D’Addario, J. L. Donovan Meyer, D. T. Emerson, A. S. Evans, P. Fisher, K. Golap, D. M. Griffith, A. E. Hale, D. Halstead, E. J. Hardy, M. C. Hatz, M. Holdaway, R. Indebetouw, P. R. Jewell, A. A.

- Kepley, D. C. Kim, M. D. Lacy, A. K. Leroy, H. S. Liszt, C. J. Lonsdale, B. Matthews, M. McKinnon, B. S. Mason, G. Moellenbrock, A. Moullet, S. T. Myers, J. Ott, A. B. Peck, J. Pisano, S. J. E. Radford, W. T. Randolph, U. Rao Venkata, M. G. Rawlings, R. Rosen, S. L. Schnee, K. S. Scott, N. K. Sharp, K. Sheth, R. S. Simon, T. Tsutsumi, S. J. Wood, The 2014 ALMA Long Baseline Campaign: An Overview, *Astrophys. J. Lett.* 808 (2015) L1. doi:10.1088/2041-8205/808/1/L1. [arXiv:1504.04877](#).
- [52] J. S. Urquhart, T. J. T. Moore, M. G. Hoare, S. L. Lumsden, R. D. Oudmaijer, J. M. Rathborne, J. C. Mottram, B. Davies, J. J. Stead, The Red MSX Source survey: distribution and properties of a sample of massive young stars, *Mon. Not. R. Astron. Soc.* 410 (2011) 1237–1250. doi:10.1111/j.1365-2966.2010.17514.x. [arXiv:1008.3149](#).
 - [53] P. Schilke, C. Comito, S. Thorwirth, F. Wyrowski, K. M. Menten, R. Güsten, P. Bergman, L. Å. Nyman, Submillimeter spectroscopy of southern hot cores: NGC 6334(I) and G327.3-0.6, *Astronom. Astrophys.* 454 (2006) L41–L45. doi:10.1051/0004-6361:20065398. [arXiv:astro-ph/0605487](#).
 - [54] F. Wyrowski, K. M. Menten, P. Schilke, S. Thorwirth, R. Güsten, P. Bergman, Revealing the environs of the remarkable southern hot core G327.3-0.6, *Astronom. Astrophys.* 454 (2006) L91–L94. doi:10.1051/0004-6361:20065347. [arXiv:astro-ph/0605667](#).
 - [55] S. E. Bisschop, P. Schilke, F. Wyrowski, A. Bellocle, C. Brinch, C. P. Endres, R. Güsten, H. Hafok, S. Heyminck, J. K. Jørgensen, H. S. P. Müller, K. M. Menten, R. Rolffs, S. Schlemmer, Dimethyl ether in its ground state, $v = 0$, and lowest two torsionally excited states, $v_{11} = 1$ and $v_{15} = 1$, in the high-mass star-forming region G327.3-0.6, *Astronom. Astrophys.* 552 (2013) A122. doi:10.1051/0004-6361/201118719. [arXiv:1302.6041](#).
 - [56] T. Müller, C. Endres, P. Schilke, eXtended CASA Line Analysis Software Suite (XCLASS), *Astronom. Astrophys.* 598 (2017) A7. doi:10.1051/0004-6361/201527203.
 - [57] H. S. P. Müller, F. Schlöder, J. Stutzki, G. Winnewisser, The Cologne Database for Molecular Spectroscopy, CDMS: a useful tool for astronomers and spectroscopists, *Journal of Molecular Structure* 742 (2005) 215–227. doi:10.1016/j.molstruc.2005.01.027.
 - [58] H. M. Pickett, R. L. Poynter, E. A. Cohen, M. L. Delitsky, J. C. Pearson, H. S. P. Müller, Submillimeter, millimeter and microwave spectral line catalog., *J. Quant. Spectrosc. Radiat. Transf.* 60 (1998) 883–890. doi:10.1016/S0022-4073(98)00091-0.
 - [59] Z. Kisiel, C. A. Nixon, M. A. Cordiner, A. E. Thelen, S. B. Charnley, Propionitrile in the two lowest excited vibrational states in the laboratory and on Titan, *J. Mol. Spectrosc.* (2020) 111324. doi:10.1016/j.jms.2020.111324.

Table 1: Summary of the individual datasets that were included in the fit.

State	max. J	max. K_a	max. Energy	# Levels	σ
$v_{12} = 1$	90	18	1731 cm ⁻¹	2141	0.96
$v_{20} = 1$	90	25	1537 cm ⁻¹	2277	0.88
$v_{13} = 1, A$	80	25	1617 cm ⁻¹	2887	1.12
$v_{21} = 1, A$	66	23	1092 cm ⁻¹	2012	0.96
Transitions	max. J	max. K_a	max. Freq.	# Trans.	σ
Ground State	130	36	1160 GHz	5259	1.03
$v_{12} = 1$	71	17	605 GHz	1578	2.76
$v_{20} = 1$	71	25	605 GHz	1338	1.69
$v_{13} = 1$	43	15	255 GHz	1244	2.92
$v_{21} = 1$	42	17	254 GHz	1068	2.86

 Table 2: Molecular parameters of CH₃CH₂CN derived from the combined fit^a.

Parameter	$v = 0$	$v_{12} = 1$	$v_{20} = 1$	$v_{13} = 1$	$v_{21} = 1$
A	27 663.681 22(79)	28 082.0334(51)	27 445.3437(37)	27 809.08(87)	27 643.22(87)
B	4714.187 49(11)	4707.357 69(22)	4715.646 15(25)	4728.844(10)	4712.789(11)
C	4235.084 92(10)	4228.628 90(21)	4240.783 39(23)	4240.6283(11)	4233.1663(11)
D_J	$\times 10^3$ 3.007 878(47)	2.980 446(80)	3.015 183(85)	3.036 48(19)	2.958 27(33)
D_{JK}	$\times 10^3$ -47.266 51(63)	-48.4881(23)	-46.5426(23)	-45.609(15)	-47.172(15)
D_K	$\times 10^3$ 547.7867(57)	602.58(12)	510.003(33)	531.03(14)	567.16(16)
d_1	$\times 10^3$ -0.685 828(10)	-0.681 012(14)	-0.683 429(15)	-0.709 74(10)	-0.663 26(12)
d_2	$\times 10^3$ -0.032 791 7(35)	-0.034 197 6(88)	-0.028 829 0(89)	-0.039 280(40)	-0.028 411(34)
H_J	$\times 10^6$ 0.009 326 7(85)	0.009 235(11)	0.009 228(12)	0.009 326 7(85)	0.008 836(66)
H_{JK}	$\times 10^6$ -0.119 08(21)	-0.109 30(33)	-0.113 72(42)	-0.119 08(21)	-0.119 08(21)
H_{KJ}	$\times 10^6$ -1.5876(13)	-2.5255(84)	-1.4433(51)	1.675(43)	-4.548(41)
H_K	$\times 10^6$ 31.373(23)	33.42(40)	25.685(60)	5.82(38)	55.22(37)
h_1	$\times 10^9$ 3.8835(20)	3.8835(20)	3.8835(20)	3.8835(20)	3.8835(20)
h_2	$\times 10^9$ 0.519 67(78)	0.519 67(78)	0.519 67(78)	0.519 67(78)	0.519 67(78)
h_3	$\times 10^9$ 0.063 32(39)	0.063 32(39)	0.063 32(39)	0.063 32(39)	0.063 32(39)
L_J	$\times 10^{12}$ -0.039 48(64)	-0.039 48(64)	-0.039 48(64)	-0.039 48(64)	-0.039 48(64)
L_{JK}	$\times 10^{12}$ 0.556(28)	0.556(28)	0.556(28)	0.556(28)	0.556(28)
L_{JK}	$\times 10^{12}$ -5.74(24)	-5.74(24)	-5.74(24)	-5.74(24)	-5.74(24)
L_{KJ}	$\times 10^{12}$ 85.42(98)	85.42(98)	85.42(98)	85.42(98)	85.42(98)
L_K	$\times 10^9$ -2.195(39)	-2.195(39)	-2.195(39)	-2.195(39)	-2.195(39)
l_1	$\times 10^{15}$ -19.10(11)	-19.10(11)	-19.10(11)	-19.10(11)	-19.10(11)
l_2	$\times 10^{15}$ -4.708(50)	-4.708(50)	-4.708(50)	-4.708(50)	-4.708(50)
l_3	$\times 10^{15}$ -1.213(29)	-1.213(29)	-1.213(29)	-1.213(29)	-1.213(29)
l_4	$\times 10^{15}$ -0.153(12)	-0.153(12)	-0.153(12)	-0.153(12)	-0.153(12)
P_J	$\times 10^{18}$ 0.106(17)	0.106(17)	0.106(17)	0.106(17)	0.106(17)
P_{JK}	$\times 10^{15}$ -0.0060(13)	-0.0060(13)	-0.0060(13)	-0.0060(13)	-0.0060(13)
P_{JK}	$\times 10^{15}$ 0.121(12)	0.121(12)	0.121(12)	0.121(12)	0.121(12)
P_{KJ}	$\times 10^{15}$ -2.04(14)	-2.04(14)	-2.04(14)	-2.04(14)	-2.04(14)
P_{KKJ}	$\times 10^{15}$ 0.165(23)	0.165(23)	0.165(23)	0.165(23)	0.165(23)
P_K	$\times 10^{12}$ 0.165(23)	0.165(23)	0.165(23)	0.165(23)	0.165(23)
D_{ab}				11.20(16)	

Note. Units are MHz. Standard errors are given in parenthesis. Parameters of the ground state are applied to all excited states and difference values are fitted for the individual excited states. Here, the ground state values and the difference values are summed up to facilitate readability. Thus, parameters among states and their uncertainty are exactly the same if no difference parameter was included. ^a Simultaneous fit to the rotation and rotation-vibration data of the $v = 0$, $v_{13} = 1$, $v_{21} = 1$, $v_{12} = 1$, and $v_{20} = 1$ states.

Table 3: State energies for the A symmetry species derived from the combined fit.

State	Symmetry	Energy [cm $^{-1}$]
$v = 0$	a'	0.0 ^a
$v_{12} = 1$	a'	532.699 617(16)
$v_{20} = 1$	a''	372.635 293(15)
$v_{13} = 1$	a'	205.934 099(8)
$v_{21} = 1$	a''	212.141 101(8)

^a Fixed.

Table 4: Tunneling Parameters for $v_{21} = 1$ and $v_{13} = 1$ obtained from the combined fit.

Parameter	SPFIT notation	$v_{21} = 1$	$v_{13} = 1$
ρ	9100vv	0.134	
ϵ_1 [MHz]	10000000vv	37.163(45)	-3.528(35)
T_1^{001} [MHz]	10000001vv	0.0489(19)	
T_1^{010} [MHz]	10000010vv	-0.016 870(68)	
T_1^{100} [MHz]	10000400vv	-0.009 499(25)	

Note. ρ was manually adjusted. See text for details. The $m k j$ values in the Fourier series coefficients $T_q^{m k j}$ determine the corresponding rotational operator $P_z^{2j} P_z^{2k} (P_+^2 - P_-^2)^m$ that is expanded and q determines the order of the Fourier series.

Table 5: Interaction parameters for $v_{21} = 1$ and $v_{13} = 1$ obtained from the combined fit.

Parameter	Operator	SPFIT notation	Value
G_a	\hat{J}_a	2000v1v2	20 122.6(40)
$G_{a,J}$	$\{\hat{J}^2, \hat{J}_a\}$	2001v1v2	0.015 90(26)
$G_{a,K}$	$\{\hat{J}_z^2, \hat{J}_a\}$	2010v1v2	-1.5197(31)
F_{bc}	$\{\hat{J}_b, \hat{J}_c\}$	2100v1v2	-0.001 371(21)
G_{2a}	$\{\hat{J}_a, (\hat{J}_b^2 - \hat{J}_c^2)\}$	2200v1v2	-0.075 55(82)
G_b	\hat{J}_b	4000v1v2	1014.94(91)
$G_{b,K}$	$\{\hat{J}_z^2, \hat{J}_b\}$	4010v1v2	-1.804(12)
F_{ca}	$\{\hat{J}_c, \hat{J}_a\}$	4100v1v2	-0.045 76(21)
G_{2b}	$\{\hat{J}_b, (\hat{J}_c^2 - \hat{J}_a^2)\}$	4200v1v2	-0.010 710(67)

Note. Units are MHz. $\{, \}$ is the anticommutator. v1, v2 are labels for the vibrational states v_{13} and v_{21} used in SPFIT. See par-file for details.